

Constraining Circumgalactic Turbulence with QSO Absorption-line Measurements

BRAD KOPLITZ ¹, EDWARD BUIE II ², AND EVAN SCANNAPIECO ¹

¹*School of Earth & Space Exploration, Arizona State University, 781 Terrace Mall, Tempe, AZ 85287, USA*

²*Physics & Astronomy Department, Vassar College, 124 Raymond Avenue, Poughkeepsie, NY 12604, USA*

ABSTRACT

Our knowledge of the circumgalactic medium (CGM) is mostly based on quasar absorption-line measurements. These have uncovered a multiphase medium that is likely highly turbulent, but constraints of this turbulence are limited to measurements of the non-thermal width of absorption-line components (b_{turb}) and the line-of-sight velocity dispersion between components (σ_{LOS}). Here we analyze a suite of CGM simulations to determine how well these indirect measures are related to the underlying CGM. Our simulations track the non-equilibrium evolution of all commonly observed ions, and consist of two main types: small-scale simulations of regions of homogeneous CGM turbulence and global simulations of inhomogeneous turbulence throughout a galactic halo. From each simulation, we generate mock spectra of Si II, Si IV, C IV, and O VI, which allow us to directly compare b_{turb} and σ_{LOS} to the true line-of-sight turbulence (σ_{1D}). In the small-scale simulations, b_{turb} is only weakly correlated with σ_{1D} , likely because it measures random motions within individual warm CGM clouds, which do not sample the overall random motions. Meanwhile, σ_{LOS} and σ_{1D} are strongly correlated, with $\sigma_{\text{1D}} \approx \sigma_{\text{LOS}} + 10 \text{ km s}^{-1}$ in the densest regions we simulated, though, the strength of this correlation depended weakly on the gas phase being probed. Our large-scale simulations also indicate that b_{turb} and σ_{1D} are largely uncorrelated, and that $\sigma_{\text{1D}} \approx \sigma_{\text{LOS}} + 10 \text{ km s}^{-1}$ on average, although it varies along individual sightlines. Moreover, the σ_{LOS} distributions from our global simulations are similar to recent observations, suggesting that this quantity may provide useful constraints on circumgalactic turbulence regardless of the axis probed.

Keywords: Circumgalactic medium (1879); Galaxy kinematics (602); Astrochemistry (75); Hydrodynamical simulations (767); Magnetohydrodynamical simulations (1966)

1. INTRODUCTION

Galaxies can only form because of the larger environment that sustains them. This circumgalactic medium (CGM) is the source of galaxies' baryonic material, and its properties are essential to determining the history of galaxy evolution. Yet observational constraints of the structure of the CGM are extremely limited.

The primary source of this information comes from absorption-line spectroscopy, with surveys such as COS-Halos (Tumlinson et al. 2013; Werk et al. 2013, 2016), the Keck Baryonic Structure Survey (KBSS; Rudie et al. 2012, 2019; Erb et al. 2022), COS-Dwarfs (Bordoloi et al. 2014), COS-GASS (Borthakur et al. 2015, 2016), and

the Cosmic Ultraviolet Baryon Survey (CUBS; Chen et al. 2020; Zahedy et al. 2021; Qu et al. 2022), using bright background quasars as light sources. Most of this work has been at restframe UV wavelengths, though some work has been done in the X-ray (e.g., Comparat et al. 2022; Nicastro et al. 2023). Observations such as these have shown that the CGM is highly ionized, extended, and multiphase, with warm ions such as C IV and Si IV being found at similar velocities as colder ions, such as Mg II, N II, and Si II (Tripp et al. 2011; Meiring et al. 2013; Burchett et al. 2015; Burchett et al. 2019). Furthermore, this cold gas is often associated with gas in higher ionization states including O VI and Ne VIII, which usually occur at physical conditions that indicate rapid cooling.

Together, these observations directly imply the presence of radically different phases in close spatial proximity and the rapid cycling of baryons amongst these

phases (e.g. Lochhaas et al. 2020). Thus, galaxy formation must be understood as embedded within a baryon cycle in which: (i) material continually cools and flows onto galaxies (e.g., Kereš et al. 2005; Dekel & Birnboim 2006; Kereš & Hernquist 2009; Stewart et al. 2011; Rubin et al. 2012; Voit et al. 2015), (ii) supernova-driven outflows put significant mass and energy back into the to the CGM (e.g., Heckman et al. 1990; Martin 2005; Veilleux et al. 2005; Steidel et al. 2010; Martin et al. 2012; Scannapieco & Brüggén 2015; Thompson et al. 2016; Scannapieco 2017; Chisholm et al. 2017; Fielding et al. 2017), and (iii) accreting black holes act as even more efficient energy sources, ejecting material into the CGM in the form of wide-angle winds and relativistic jets (Scannapieco & Oh 2004; Di Matteo et al. 2005; Croton et al. 2006; Thacker et al. 2006; McNamara & Nulsen 2007; Moe et al. 2009; Hamann et al. 2011; Fabian 2012; Arav et al. 2013).

All of these processes drive significant turbulence, which is likely to exist at levels that alter the properties of the CGM. In fact, the CGM is particularly sensitive to turbulent motions, as rapid cooling lowers the temperature of much of the medium to significantly below the virial temperature. This means that random motions on the order of ≈ 0.25 the virial velocity, as observed in galaxy groups and clusters (e.g., Werner et al. 2009; Hitomi Collaboration et al. 2016; Ogorzalek et al. 2017; Zhuravleva et al. 2018; Eckert et al. 2019), can give rise to supersonic motions in the CGM. The resulting shocks can produce density and temperature structures that are dependent on the average turbulent Mach number (Buie et al. 2020a), strongly affecting the baryon cycle and its impact on galaxy formation.

Accurately capturing these processes in cosmological simulations presents two major challenges. First, simulating the CGM at sufficient resolution to follow turbulent motions in a cosmological setting can be very computationally expensive (e.g., Hummels et al. 2019; Peebles et al. 2019; van de Voort et al. 2019; Lochhaas et al. 2022). Second, the large uncertainties in the turbulent properties of the CGM make it difficult to sufficiently span the parameter space allowed by current observations.

This uncertainty arises because, unlike in galaxy clusters, the scale at which turbulence is probed by observations may differ substantially from the scale at which it is driven. CGM measurements of turbulence consist of two main types: (i) the turbulent broadening associated with the line profile of individual absorbers, and (ii) the distribution of the velocity centroids of absorption-line systems relative to one another. While both of these types of measurements provide constraints on random

velocities, these are also both likely to underestimate the total level of turbulence. This is due to the turbulent cascade causing the velocities to be distributed as a function of scale, as $v(L) \propto (L/L_{\text{drive}})^\alpha$, where $1/3 \leq \alpha \leq 1/2$ depends on the Mach number of the medium (Kritsuk et al. 2007; Pan & Scannapieco 2010). As a result, understanding how well observational tracers recover the turbulent velocities requires a careful comparison between observations and simulations.

Motivated by these issues, we undertake a comprehensive investigation to quantify how observational measurements of turbulence are related to the underlying CGM kinematics. Our study builds on the work of Buie et al. (2018, 2020b, 2022), who carried out a large suite of idealized simulations to model the impact of turbulence on the properties of the CGM. These were of two types: (i) small-scale simulations of regions of homogeneous CGM turbulence, and (ii) global simulations of inhomogeneous turbulence that was driven in a galactic halo with gravitational acceleration and co-rotation. Here we make use of both types of simulations to investigate the motions inferred from the two most common estimators of turbulence and compare them to the true values of the random motion in these simulations.

The structure of this paper is as follows: §2 introduces the simulations we analyze, §3 shows how we generate spectra from sightlines through the simulations, and §4 details how we estimate the amount of turbulence present in individual components and along sightlines. §5 presents the results of our analysis, quantifying the relationship between true and inferred turbulent motions. A summary and conclusions are given in §6.

2. MAIHEM SIMULATIONS

The simulations we analyze make use of the open-source Models of Agitated and Illuminated Hindering and Emitting Media (MAIHEM¹) code to model turbulence in the CGM. MAIHEM is a three-dimensional (3D) cooling and chemistry package built using FLASH (Version 4.3; Fryxell et al. 2000). The version we used tracks the reaction network of 65 ions: hydrogen (H I and H II), helium (He I – He III), carbon (C I – C VI), nitrogen (N I – N VII), oxygen (O I – O VIII), neon (Ne I – Ne X), sodium (Na I – Na III), magnesium (Mg I – Mg IV), silicon (Si I – Si VI), sulfur (S I – S V), calcium (Ca I – Ca V), iron (Fe I – Fe V), and electrons. For each of these species, the code tracks collisional ionizations by electrons, photoionizations by a UV background, dielectric and radiative recombinations, and charge transfer

¹ <http://maihem.asu.edu/>

reactions. MAIHEM was developed in Gray et al. (2015) and later expanded upon in Gray & Scannapieco (2016) and Gray & Scannapieco (2017). The simulations analyzed in this work were run with a $0.3 Z_{\odot}$ metallicity and exposed to a Haardt & Madau (2012) extragalactic UV background at $z = 0$.

2.1. Small-Scale Simulations

To understand turbulence in the CGM on small scales, we analyze the homogenous box simulations by Buie et al. (2018). Turbulence is driven in these simulations through the use of an artificial forcing term \mathbf{F} incorporated into the momentum equation as

$$\frac{\partial \rho \mathbf{v}}{\partial t} + \nabla(\rho \mathbf{v} \mathbf{v}) + \nabla P = \rho \mathbf{F}, \quad (1)$$

where ρ is the density, P is the pressure, and \mathbf{v} is the velocity. The forcing term was modeled as a stochastic Ornstein-Uhlenbeck process (Uhlenbeck & Ornstein 1930; Schmidt et al. 2009; Federrath et al. 2010; Pan & Scannapieco 2010) with a user-defined forcing correlation time t_f , approximately equal to the eddy turnover time. For all the simulations presented here, turbulence was driven solely through solenoidal modes (i.e., $\nabla \cdot \mathbf{F} = 0$) in the range of wavenumbers $1 \leq L_{\text{box}} |\mathbf{k}| / 2\pi \leq 3$, such that the average forcing wavenumber was $k_f^{-1} \simeq 2L_{\text{box}} / 2\pi$, with L_{box} the size of our turbulent box, which was fixed at 100 parsecs on a side. This turbulence was continuously driven throughout the simulation runtime.

The parameter space spanned by the simulations is greatly simplified by the dependencies of turbulent decay and cooling on density and length scale. In particular, the simulations are invariant under transformations in which $x \rightarrow \lambda x$, $t \rightarrow \lambda t$, and $\rho \rightarrow \rho / \lambda$. This means that the species fractions and thermal state of the gas will only depend on the ionization parameter (U), σ_{1D} , and the product of the mean density and the turbulent driving scale, nL_{drive} . Here $U \equiv \frac{\Phi}{n_{\text{H}} c}$, where Φ is the total flux of ionizing photons, n_{H} is the total hydrogen density, and c is the speed of light. The simulations we analyze have $\log U$ between -3 and -1 which matches the observations of the COS-Halos survey (Werk et al. 2014).

We considered turbulence driven to one-dimensional velocity dispersions of $\sigma_{1D} = 6, 17, 26, 35, 46$, and 58 km s^{-1} and $n = 0.1, 1$, and 10 cm^{-3} . With the range of driving modes described above, each simulation has an average driving scale of $L_{\text{drive}} \approx 40 \text{ pc}$ leading to $nL_{\text{drive}} \approx 10^{19}, 10^{20}$, and 10^{21} cm^{-2} . Each simulation was started with a uniform density and temperature $T = 10^5 \text{ K}$, which is roughly the density and temperature of various phases within the CGM (Tumlinson et al.

2017). These simulations have a resolution of 128^3 , corresponding to 0.8 pc , and they were evolved until reaching a steady state solution. As a result, the duration of each run varies.

In Figure 1, we show temperature slices through the $nL_{\text{drive}} = 10^{20} \text{ cm}^{-2}$ boxes as an example of how the small-scale simulations look. At lower turbulent velocities ($\sigma_{1D} \leq 26 \text{ km s}^{-1}$), the gas is subsonic, yielding weak shocks and small temperature gradients. At higher velocity dispersions, we begin to see larger temperature gradients caused by stronger shocks. These sweep across cells carrying newly-ionized material in their wakes and lead to a large spread in the range of species formed in the simulations. Note also how the structures change from more cloud-like at low Mach numbers, to more planar at high Mach numbers, as α , the slope of the turbulent cascade becomes steeper and the fractal dimension of the velocity field changes (e.g., Pan & Scannapieco 2011).

In Figure 2, we show temperature slices through each box with $\sigma_{1D} = 46 \text{ km s}^{-1}$ to indicate how changing nL_{drive} impacts the simulated gas. By decreasing nL_{drive} , we reduce the eddy turnover time, which increases the energy input rate and the temperature. Thus, decreasing decreasing nL_{drive} , produces a higher level of ionization in the gas.

A detailed discussion of all the small-scale simulations used in this study can be found in Buie et al. (2018). Additional simulations were also run by Buie et al. (2018) at lower densities, but these either: (i) failed to achieve a steady state, leading to thermal runaway, or (ii) failed to produce N above our cutoff of 10^{11} cm^{-2} , as discussed below in §4.1. As a result, we exclude them from our analysis.

2.2. Large-Scale Simulations

We also consider two large-scale simulations from Buie et al. (2022). Each was run with the same initial conditions except that one followed the equations of magnetohydrodynamics, which we refer to as the MHD run, and one did not include magnetic fields, which we refer to as the Hydro run. These simulations were carried out in $(800 \text{ kpc})^3$ sized boxes with turbulence injected as a function of radius from the simulation center such that

$$a_{x,y,z} = a_{x,y,z}^0 \left(\frac{r + 0.3 R_{\text{vir}}}{0.5 R_{\text{vir}}} \right)^{-1}, \quad (2)$$

where $a_{x,y,z}^0$ is the central acceleration and R_{vir} is the virial radius of the simulated galaxy.

Additionally, the initial gas density was chosen to follow an Navarro et al. (1996, NFW) profile with a dark

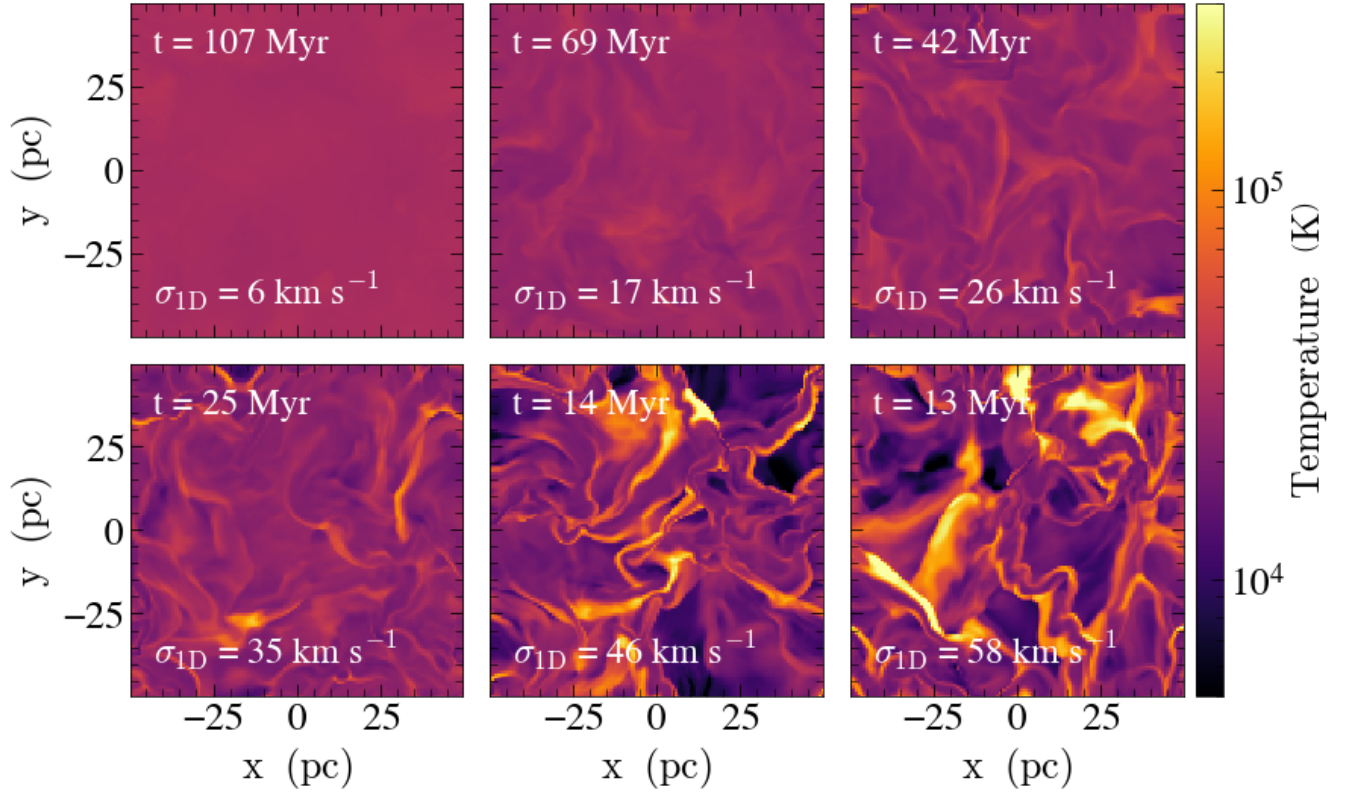


Figure 1. Temperature slices in the xy -plane through the $nL_{\text{drive}} = 10^{20} \text{ cm}^{-2}$ density small-scale simulations. The injected σ_{1D} is shown in the lower left of each panel. The upper left shows the amount of time each simulation was ran for.

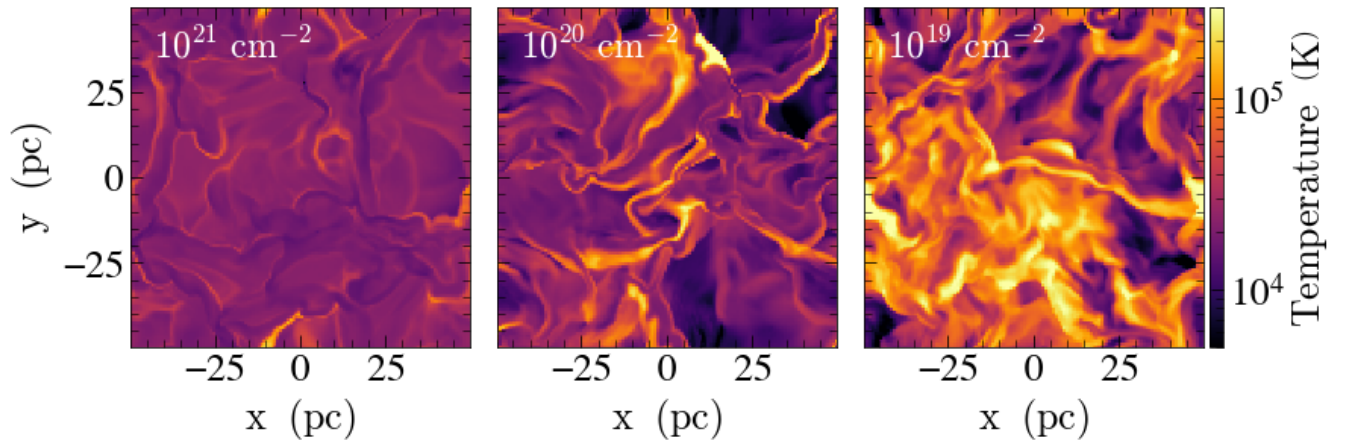


Figure 2. Temperature slices in the xy -plane through each simulation with $\sigma_{1D} = 46 \text{ km s}^{-1}$. The upper left of each panel shows the nL_{drive} of the simulation being shown.

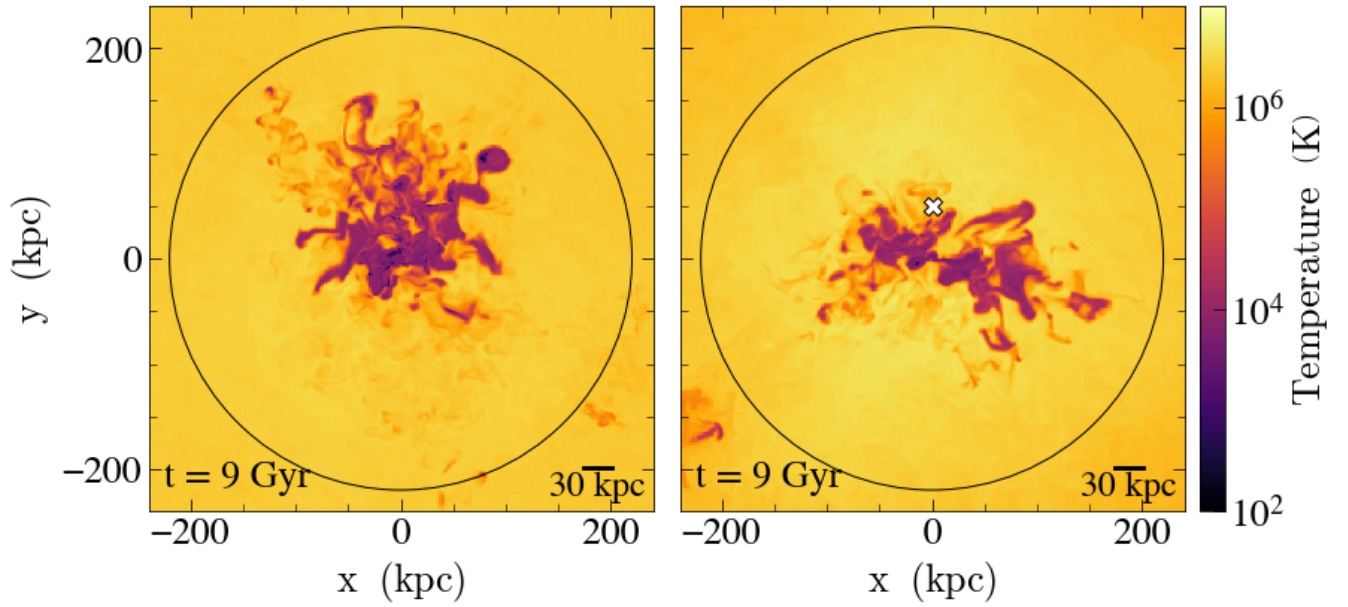


Figure 3. Temperature slices in the xy -plane through the Hydro (left) and MHD (right) simulations after 9 Gyr of evolution. The virial radius of the simulation is shown by a black circle. The white X shows the position of the example sightline shown in Figure 4. Each simulation ran for 9 Gyr, which we show in the lower left of each panel.

matter halo described by

$$\rho(r) = \frac{\rho_0}{\frac{r}{R_s} \left(1 + \frac{r}{R_s}\right)^2}, \quad (3)$$

where $\rho_0 \equiv M_{\text{halo}} \{4\pi R_s^3 [\ln(1+c) - c(1+c)^{-1}]\}^{-1}$ is the central dark matter density, $R_s = R_{\text{vir}}/c$ is the scale radius, and c and M_{halo} are the concentration parameter and halo mass. The simulations we investigate here were run for 9 Gyr with $R_{\text{vir}} = 220$ kpc, $c = 10$, and $M_{\text{halo}} = 10^{12} M_{\odot}$. The virial temperature in this case is $\approx 1.2 \times 10^6$ K, corresponding to a sound speed of ≈ 170 km s $^{-1}$.

The L_{drive} of the simulations were chosen to be 30 kpc, which is approximately the size of the Milky Way disk. This led to nL_{drive} values which are comparable to the small-scale simulations. Additionally, each cell in the simulations was exposed to the same extragalactic UV background (Haardt & Madau 2012). This, combined with the initial density profiles described above, led to the initial ionization fraction varying from 10^{-8} in the simulated galaxy, to 10^{-5} just outside the galaxy, and 0.9 in the outer regions of the CGM. A refined mesh grid was used for these large-scale simulations. Our sightlines probe these boxes within R_{vir} of the center, where the resolution is highest with 512^3 , corresponding to 1.6 kpc.

The magnitude of the turbulent driving was set such that the initial average turbulent motion is ≈ 45 km s $^{-1}$ within the virial radius, but additional convective motions are generated as the simulation evolves, increasing the overall turbulence at late times. In both simulations, we initialized the medium with a Keplerian circular velocity modified by the observational findings from the Mg II studies of Ho et al. (2017), using their Equation (A2) to set how velocities should fall off along the minor axis, which is chosen to be the y -axis in our runs. This gives a rotational velocity of

$$v_{\text{rot}} = f_{\text{rot}} \sqrt{\frac{4\pi G r^2 \rho_{\text{NFW}}(r)}{3}} H_s(y), \quad (4)$$

where G is the gravitational constant, $H_s \equiv \exp(-|y|/50 \text{ kpc})$, and f_{rot} is an overall scaling parameter set to 60%. In the MHD case, the simulation included a uniform seed magnetic field in the z -direction of $0.1 \mu\text{G}$ run. We refer the reader to Buie et al. (2020b) and Buie et al. (2022) for additional details on the simulations.

We analyzed each simulation after 9 Gyr of evolution, and measured the turbulent profile in detail as discussed in §5.2. In Figure 3, we show temperature slices in the xy -plane through the Hydro (left) and MHD (right) simulations. At this time, most of the volume is filled

with a diffuse ambient medium and dense structures, such as clouds and filaments. The Hydro run tends to have a slightly wider range of temperatures, such that a significant population of cold clumps can be seen at temperatures down to a few hundred degrees. In the MHD simulation, however, the temperature range is more limited, likely due to the presence of magnetic pressure, which puffs up the clumps reducing their overall cooling. At the same time, magnetic fields aid in the transport of angular momentum, such that the overall population of dense $10^2 - 10^4$ K gas is closer to the center in the MHD run.

3. GENERATING MOCK OBSERVATIONS

Our simulated absorption-line observations are generated by calculating the optical depth as a function of frequency (ν) in each grid cell along the sightlines as

$$\tau_{\nu} = \int n_X x^{n+} \sigma_{\nu} d\nu, \quad (5)$$

where n_X is the number density of element X and x^{n+} is the fraction of element X atoms in the n th ionization state. We calculate τ_{ν} in each cell along the sightline, summing all cells together to get the total optical depth. Here the absorption cross section (σ_{ν}) can be expressed as

$$\sigma_{\nu} = \frac{\pi e^2}{m_e c} f_{lu} \phi_{\nu}, \quad (6)$$

where e and m_e are the charge and mass of an electron, respectively, f_{lu} is the oscillator strength of the transition (Morton 2003), and the line profile (ϕ_{ν}) is a Gaussian of the form:

$$\phi_{\nu} = \frac{1}{\Delta\nu_D \sqrt{\pi}} \exp\left[-\left(\frac{\nu - \nu_{lu}}{\Delta\nu_D}\right)^2\right], \quad (7)$$

where

$$\Delta\nu_D \equiv \frac{\nu_{lu}}{c} b_X = \frac{\nu_{lu}}{c} \sqrt{\frac{2k_B T}{m_X}}, \quad (8)$$

k_B is the Boltzmann constant, and m_X and b_X are the mass and Doppler width of element X , respectively.

To simulate observations taken with Cosmic Origins Spectrograph (COS) aboard the Hubble Space Telescope (HST), we convolve the resulting spectrum with an 8 km s $^{-1}$ wide Gaussian profile (Osterman et al. 2011). We show an example sightline through the large-scale MHD box in the left panel of Figure 4, which probes the halo at an impact parameter of $\rho = 50$ kpc at the position indicated in Figure 3 with a white X.

4. INFERRING TURBULENT VELOCITIES

4.1. Fitting Voigt Profiles

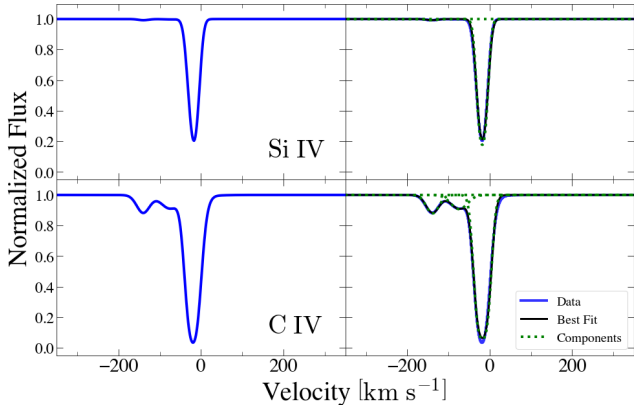


Figure 4. Example spectrum of Si IV (top) and C IV (bottom) through the large-scale MHD simulation with $\rho = 50$ kpc is shown in the left panel. The position of this example sightline is shown in Figure 3 as a white X. The resulting Voigt profile fits from RBVfit are shown in the right panels.

Once the absorption lines have been generated, we fit them to Voigt profiles using the Bayesian fitting code RBVfit², which takes in a normalized spectrum and returns the best-fit column density (N), Doppler width parameter (b), and velocity centroid (v) of each absorption feature along with the associated uncertainties. An example of these fits is shown in the right panels of Figure 4.

We limit our analysis to components with $N \geq 10^{11}$ cm^{-2} . This limit was chosen to be below the observational limit of COS ($N \approx 10^{12}$ cm^{-2} ; Tumlinson et al. 2017) and above $N \approx 10^{10}$ cm^{-2} , where the uncertainties became so large that the returned values were unreliable.

While all of our simulated ions have multiple UV transitions, we only consider the stronger line of each ion. Each line will have the same shape but differ by the depth of the absorption feature according to the relative oscillator strengths. Therefore, little information can be gained from generating and fitting all lines in a transition.

4.2. Turbulent Velocity Measures

Our Voigt profile fits allow us to measure turbulence in multiple ways. With the Doppler b parameters of C IV and Si IV, we are able to determine the turbulence in individual components while the v of each ion can be used to find the turbulence along the entire sightline. Since each measure uses different parameters, they are independent tracers of the turbulence.

² <https://github.com/rongmon/rbvfit>

Following Rauch et al. (1996), we use C IV ($\lambda\lambda 1548, 1550$ Å) and Si IV ($\lambda\lambda 1393, 1402$ Å) to separate the observed line profiles into thermal and turbulent or “non-thermal” components. To do this we assume that b values can be expressed as a thermal component (b_{therm}) and a non-thermal or turbulent component (b_{turb}):

$$b_X^2 = b_{\text{therm},X}^2 + b_{\text{turb}}^2 = \frac{2k_B T}{m_X} + b_{\text{turb}}^2, \quad (9)$$

where X is either C IV or Si IV for our analysis. These equations can be rearranged to give:

$$b_{\text{turb}}^2 = \sqrt{b_{\text{CIV}}^2 - b_{\text{therm,CIV}}^2}, \quad (10)$$

and

$$b_{\text{therm,CIV}} = \frac{b_{\text{CIV}}^2 - b_{\text{SiIV}}^2}{1 - (m_{\text{C}}/m_{\text{Si}})}, \quad (11)$$

which allows us to deconvolve b_{therm} from b_{turb} of the Doppler parameter and determine the turbulence in each component. This measure has been used to constrain the turbulence in individual absorbers along quasar sightlines (e.g., Rauch et al. 1996; Rudie et al. 2019).

The turbulence along the entire sightline can be probed by measuring the line-of-sight velocity dispersion, σ_{LOS} is defined as

$$\sigma_{\text{LOS}}^2 = \langle [v - \langle v \rangle]^2 \rangle, \quad (12)$$

where the angled brackets indicate taking the mean. σ_{LOS} has been used to observationally constrain the amount of turbulence along quasar sightlines (e.g., Zhu et al. 2014; Borthakur et al. 2016; Huang et al. 2016). In addition to the warm transitions of C IV and Si IV, we generate spectra of cool (Si II; $\lambda\lambda 1260, 1193, 1190, 1304$ Å) and hot (O VI; $\lambda\lambda 1032, 1037$ Å) transitions, also using them to measure σ_{LOS} . This allows us to quantify how turbulence impacts the different phases of the CGM.

Currently, observers use b_{turb} and σ_{LOS} to constrain the amount of turbulence in the universe; however, the robustness of the methods have not been well tested. To that end, we investigate these measures in MAIHEM simulations in which the “true” turbulent velocities are known.

5. RESULTS & DISCUSSION

5.1. Small-Scale

The mean and spread of our turbulent measures through each small-scale simulation are given in Table 1. Simulations without σ_{LOS} values indicate that only one

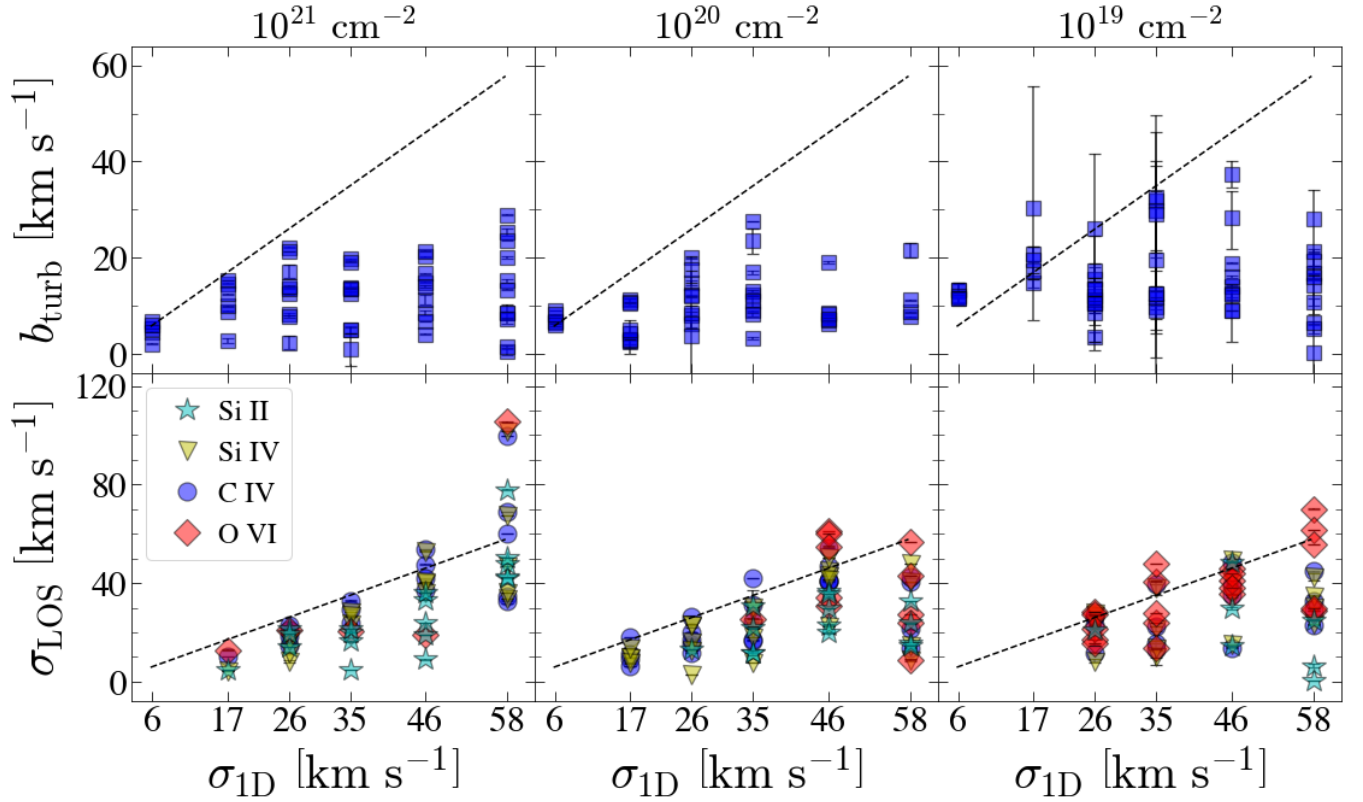


Figure 5. Turbulent measures in the small-scale simulations as a function of injected σ_{1D} , where the top panels show b_{turb} and the bottom panels are σ_{LOS} . Each column is labeled with the nL_{drive} of the box the results are through. The coloring and symbol in the top panel indicates the ion being shown with C IV being blue circles, yellow triangles for Si IV, O VI are red diamonds, and Si II shown as cyan stars. The dashed black line in each panel shows the 1-to-1 line in each panel.

component was seen in each sightline and so σ_{LOS} could not be measured. Similarly, if we could only measure σ_{LOS} for one sightline, we do not report a spread. In each of the simulations with $\sigma_{1D} = 6 \text{ km s}^{-1}$, no sightline had more than one component meaning we are not able to calculate σ_{LOS} for any of these simulations.

Figure 5 shows the measured b_{turb} (top panels) and σ_{LOS} (bottom panels) for each simulation as a function of input σ_{1D} . Each column corresponds to a different density box, as labeled at the top. In each panel, we show the 1-to-1 relation as a black dashed line. Each simulation produced at least 5 total absorbers of each ion, with as many as 23, 16, 18, and 22 being found in a single box for Si II, Si IV, C IV, and O VI, respectively. The simulations with larger σ_{1D} injected produced more components than those with smaller velocities. The sightlines used to derive the σ_{LOS} values contained 2 to 4 absorbers, on average. While a single sightline had 8 absorbers, the rest had 6 or fewer.

All components were found to have $b_{\text{turb}} < 40 \text{ km s}^{-1}$, with the vast majority ($\approx 85\%$) being narrower than 20 km s^{-1} . In addition, as σ_{1D} increases, the median b_{turb} remain relatively flat. This can be seen in the best-

fit lines, which were

$$b_{\text{turb}} = (0.135 \pm 0.003)\sigma_{1D} + (7.69 \pm 4.23), \quad (13)$$

$$b_{\text{turb}} = (0.067 \pm 0.005)\sigma_{1D} + (6.85 \pm 6.42), \quad (14)$$

$$b_{\text{turb}} = (0.013 \pm 0.006)\sigma_{1D} + (14.49 \pm 7.37), \quad (15)$$

for $nL_{\text{drive}} = 10^{21}$, 10^{20} , and 10^{19} cm^{-2} , respectively. Performing Kendall τ tests of these samples gave coefficients of 0.467, 0.333, and 0.200. These suggest that b_{turb} may not be able to accurately infer the amount of turbulence that is present on small scales.

This is likely because this quantity measures turbulence on the scale of individual warm clouds within the larger CGM, which do not sample the overall random motions that exist on larger scales. Moreover, as the dissipation of turbulence leads to heating, the level of turbulence within a given cloud is likely to be correlated with the cloud temperature, and hence with the presence of the ions we are using to measure it. Our results imply that these effects are strong enough to make b_{turb} much more dependent on the typical conditions that support the existence of C IV and Si IV than on the global turbulent properties of the medium.

Table 1. Mean turbulence results through the small-scale simulations.

σ_{1D}	b_{turb}	b_{therm}	σ_{LOS} (Si II)	σ_{LOS} (Si IV)	σ_{LOS} (C IV)	σ_{LOS} (O VI)
[km s ⁻¹]	[km s ⁻¹]	[km s ⁻¹]	[km s ⁻¹]	[km s ⁻¹]	[km s ⁻¹]	[km s ⁻¹]
$nL_{\text{drive}} = 10^{21} \text{ cm}^{-2}$ Simulations						
6	5.1 ± 1.8	13.7 ± 0.4	---	---	---	---
17	10.7 ± 4.6	12.6 ± 0.6	4.6	4.4	10.1	12.7
26	13.3 ± 6.4	12.5 ± 5.5	18.2 ± 3.8	13.5 ± 4.3	19.2 ± 3.5	20.8
35	11.5 ± 6.5	13.3 ± 3.7	15.6 ± 7.6	26.1 ± 2.3	28.7 ± 4.6	20.3
46	13.2 ± 5.9	14.5 ± 4.1	24.2 ± 10.9	42.4 ± 7.4	45.0 ± 7.2	19.0
58	14.0 ± 9.6	10.2 ± 3.9	52.2 ± 14.8	57.2 ± 28.2	59.2 ± 27.7	105.4
$nL_{\text{drive}} = 10^{20} \text{ cm}^{-2}$ Simulations						
6	7.4 ± 1.3	10.6 ± 0.3	---	---	---	---
17	6.4 ± 3.9	11.4 ± 3.5	---	10.2 ± 2.6	11.1 ± 4.9	---
26	11.5 ± 5.4	10.5 ± 1.8	13.1	15.4 ± 8.5	18.1 ± 5.5	---
35	13.9 ± 7.7	11.3 ± 3.8	18.9 ± 9.1	21.4 ± 9.1	26.2 ± 10.6	25.4
46	9.4 ± 4.8	11.4 ± 1.5	28.9 ± 7.5	40.3 ± 10.5	44.7 ± 6.0	48.2 ± 14.6
58	12.4 ± 6.4	11.0 ± 0.4	21.6 ± 8.6	27.9 ± 19.1	29.4 ± 14.3	32.0 ± 18.4
$nL_{\text{drive}} = 10^{19} \text{ cm}^{-2}$ Simulations						
6	12.3 ± 0.9	6.1 ± 1.9	---	---	---	---
17	20.6 ± 5.9	7.6 ± 3.1	---	---	---	---
26	13.0 ± 5.7	10.8 ± 3.3	20.8	21.6 ± 9.1	22.0 ± 7.0	22.0 ± 5.7
35	19.9 ± 9.9	12.9 ± 3.9	---	20.8 ± 12.3	22.6 ± 12.0	30.7 ± 13.7
46	17.6 ± 9.5	10.9 ± 9.7	30.9 ± 17.1	34.7 ± 14.5	34.0 ± 14.7	40.9 ± 4.2
58	13.9 ± 8.3	13.2 ± 7.2	10.6 ± 12.9	32.7 ± 8.0	32.1 ± 9.3	49.2 ± 18.9

The uncertainties show the standard deviation on the distribution. Simulations for which σ_{LOS} could only be measured along one sightline do not have an associated standard deviation. Blank entries show simulations where we were unable to measure σ_{LOS} along any sightline.

On the other hand, σ_{LOS} does a much better job tracing σ_{1D} . In this case

$$\sigma_{\text{LOS}} = (1.005 \pm 0.002)\sigma_{1D} + (9.68 \pm 2.94), \quad (16)$$

$$\sigma_{\text{LOS}} = (0.501 \pm 0.091)\sigma_{1D} + (4.23 \pm 139.80), \quad (17)$$

$$\sigma_{\text{LOS}} = (0.336 \pm 0.092)\sigma_{1D} + (14.69 \pm 169.60), \quad (18)$$

for $nL_{\text{drive}} = 10^{21}$, 10^{20} , and 10^{19} cm^{-2} , respectively, and Kendall τ tests of these samples gave coefficients of 1.00, 0.8, and 0.34, respectively. This means that although the random motions within individual warm clouds are not well correlated with the overall turbulent velocity, the level of random motions *between* pairs of warm clouds is strongly correlated with overall turbulence. This is likely because the relative velocities of clouds are able to sample random motions on scales much larger than the clouds themselves, providing a good estimate of the overall level of turbulence in the system.

Looking at each gas phase independently shows that the best tracer of σ_{1D} depends on the density of the gas. $\sigma_{\text{LOS}}(\text{O VI})$ followed σ_{1D} in the 10^{19} cm^{-2} density box while $\sigma_{\text{LOS}}(\text{Si II})$ produced an anti-correlation with increasing σ_{1D} . In the 10^{21} cm^{-2} density box, however, $\sigma_{\text{LOS}}(\text{Si II})$ was able to trace σ_{1D} just as well as $\sigma_{\text{LOS}}(\text{C IV})$ and $\sigma_{\text{LOS}}(\text{Si IV})$. Meanwhile, $\sigma_{\text{LOS}}(\text{C IV})$ and $\sigma_{\text{LOS}}(\text{Si IV})$ did equally well in the 10^{20} cm^{-2} density simulation.

To determine if these results are robust to viewing angle, we generated additional sightlines through these simulations along all three directions. The b_{turb} and σ_{LOS} values were consistent regardless of the axis probed, which is expected for these homogeneous simulations.

5.2. Large-Scale

Table 2. Mean turbulence results through the large-scale simulations.

ρ	b_{turb}	b_{therm}	σ_{LOS} (Si II)	σ_{LOS} (Si IV)	σ_{LOS} (C IV)	σ_{LOS} (O VI)
[kpc]	[km s ⁻¹]	[km s ⁻¹]	[km s ⁻¹]	[km s ⁻¹]	[km s ⁻¹]	[km s ⁻¹]
MHD Simulation						
0	34.3 ± 19.6	16.8 ± 14.1	100.2	67.9	74.2	39.2
10	15.3 ± 8.4	23.4 ± 8.2	78.0 ± 21.3	72.2 ± 21.9	73.7 ± 16.3	77.0 ± 14.4
14	14.5 ± 9.5	16.5 ± 7.1	64.9 ± 13.5	77.1 ± 21.3	81.4 ± 13.6	87.9 ± 17.3
25	18.3 ± 12.4	24.0 ± 23.2	71.0 ± 11.0	78.7 ± 39.8	58.9 ± 19.8	66.5 ± 19.3
35	15.7 ± 8.7	16.1 ± 9.6	49.9 ± 27.4	57.9 ± 27.9	58.8 ± 26.9	50.7 ± 21.2
50	11.3 ± 4.8	17.2 ± 8.3	38.0 ± 2.3	60.7 ± 8.6	55.2 ± 3.8	38.7 ± 20.2
71	8.1 ± 3.2	16.8 ± 4.7	49.1 ± 19.8	54.6 ± 9.0	39.6 ± 18.3	58.8 ± 17.0
75 – 110	12.0 ± 5.0	14.2 ± 7.1	32.7 ± 23.5	35.1 ± 26.8	35.0 ± 28.7	35.1 ± 22.9
Hydro Simulation						
0	16.9 ± 11.2	17.8 ± 11.4	127.5	132.9	131.0	152.2
10	11.2 ± 5.7	13.4 ± 8.7	70.3 ± 16.8	84.8 ± 15.1	83.1 ± 18.6	100.9 ± 7.5
14	10.1 ± 2.1	15.8 ± 8.6	73.4 ± 29.4	109.0 ± 32.1	107.6 ± 32.1	123.1 ± 10.0
25	10.6 ± 5.6	12.4 ± 6.5	85.0 ± 26.0	82.7 ± 16.9	82.7 ± 17.4	80.4 ± 27.8
35	9.9 ± 3.6	13.1 ± 6.3	75.6 ± 20.2	79.5 ± 19.8	82.1 ± 17.6	87.0 ± 20.1
50	12.6 ± 4.9	17.9 ± 7.0	53.0 ± 30.7	56.8 ± 21.2	59.2 ± 19.8	69.8 ± 22.7
71	12.0 ± 7.9	14.3 ± 6.5	25.3 ± 20.0	29.9 ± 16.0	28.2 ± 15.0	24.7 ± 9.1
75 – 110	9.4 ± 3.8	19.2 ± 13.3	33.1 ± 17.2	38.8 ± 16.3	41.6 ± 14.0	43.0 ± 25.1

The upper results correspond to the MHD simulation while the lower results are for the Hydro simulation with the uncertainties showing the standard deviation on the distribution. The uncertainties show the standard deviation on the distribution. At the simulation center, there is only one possible sightline and so are unable to report a distribution for the σ_{LOS} results.

While the small-scale simulations tell us about how turbulence impacts individual CGM regions, the large-scale simulations allow us to investigate the more global properties of CGM turbulence. Our sightlines probe these simulations at impact parameters within 110 kpc of their centers ($\rho / R_{\text{vir}} \leq 0.5$). Beyond this limit, C IV and Si IV were not abundant enough to measure b_{turb} robustly and so they are not included in our analysis. The radial extent of our sightlines is comparable to what most absorption studies of the CGM have access to (Tumlinson et al. 2013; Bordoloi et al. 2014; Borthakur et al. 2015), although occasionally observations are available at or beyond R_{vir} .

In Table 2 we report the average and spread of the turbulent measures in each of our simulations as a function of impact parameter. Here we bin the sightlines with $75 \leq \rho < 110$ kpc so that a similar number of sightlines and components were used to calculate the values in each row. At impact parameters of $\rho < 50$ kpc, the Hydro box produced nearly 2 more components per sightline than the MHD simulation, while both runs produced a similar number of components at larger radii.

This difference is likely due to the fact that magnetic pressure causes the colder regions to be more puffed up in the MHD simulation, as seen in Figure 3, and this leads to lower overall columns. As discussed in (Bue et al. 2022) in the MHD simulation such dynamically important fields arise only within ≈ 50 kpc of the center of the halo (see Figure 10 in that work), explaining why the differences we see here are confined to $\rho \lesssim 50$ kpc. Sightlines through the Hydro simulation produced 124 Si II absorbers, 155 Si IV absorbers, 165 C IV absorbers, and 163 O VI absorbers while the MHD simulation produced 110, 138, 142, and 122, respectively.

The right column of Figure 6 shows the b_{turb} measured for each large-scale simulation along the z -axis as a function of ρ , with the Hydro box in the top panel and the MHD box in the bottom panel. Both simulations produced clouds with $b_{\text{turb}} \leq 20$ km s⁻¹ at all ρ , and several components with large b_{turb} were found at $\rho \lesssim 35$ kpc, i.e., where the amount of injected turbulence is highest. In the MHD simulation, 5 components had $b_{\text{turb}} \geq 40$ km s⁻¹ while none were found in the small-scale or Hydro simulations with such large turbulent ve-

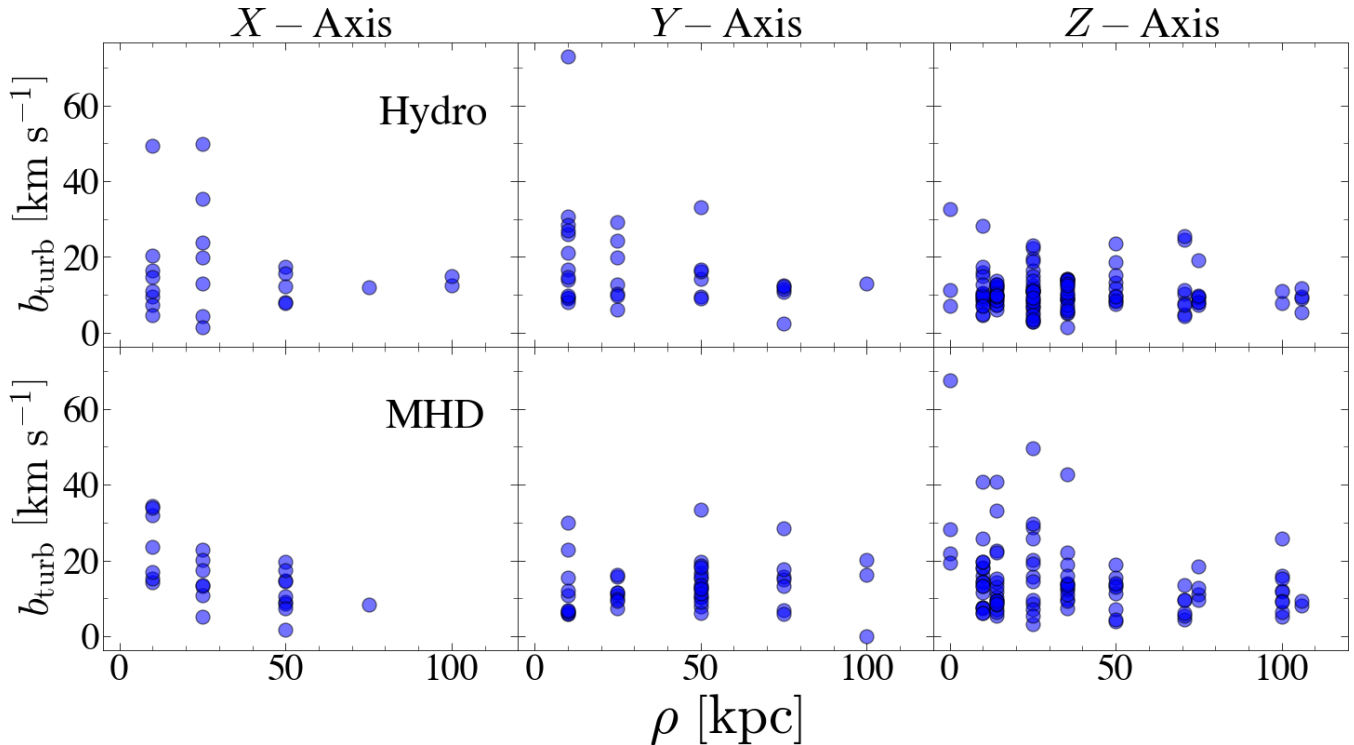


Figure 6. Component turbulent measure, b_{turb} , in the large-scale simulations as a function of distance from the center of the simulation, ρ . Results through the Hydro box are shown on the top panel while the MHD results are on the bottom. Each column corresponds to a different axis being probed by the sightlines, where y is along the axis of rotation, and x and z are perpendicular to it. Sightlines along the x -axis and y -axes are a subset of those along the z -axis and so fewer points are present in these panels.

locities. In fact, the Hydro simulation nearly always produced components with smaller b_{turb} velocities than the MHD simulation. Again this difference is likely related to the fact that the colder regions are more puffed up in this simulation, and thus they experience the larger turbulent velocities that arise at larger physical scales. This is consistent with the fact that the distribution of b_{turb} values in the two runs become similar at large radii where magnetic effects are negligible, leading to a slight anti-correlation between b_{turb} and ρ in the MHD run.

Our large-scale MHD simulation also produced a similar fraction of sightlines with $b_{\text{turb}} = 20 - 40 \text{ km s}^{-1}$ as the small-scale simulations ($\approx 13\%$ compared to $\approx 16\%$ in the small-scale simulations). In both large-scale simulations, the distribution of b_{turb} is dominated by the components with the smallest velocities $\approx 82\%$ as compared to $\approx 85\%$ for the small-scale simulations. From these results, it is clear that b_{turb} does not provide a good tracer of the true turbulent velocities.

The bottom row of Figures 7 and 8 shows our measurements of σ_{LOS} from the Hydro and MHD simulations, respectively, as a function of ρ . Here each column shows the results of a different ion, labeled in order of increasing ionization potential. To determine the amount

of turbulence as a function of radius, we directly measured the volume average, or “true”, σ_{LOS} using all the cells which have temperatures $< 10^5 \text{ K}$ and at the same projected radius from the center of the simulations, generating straws in the axis being probed. For each radius, we computed the volume average radial velocity and the volume average rotational velocity. We then subtracted these from each cell to leave only the random component of the line-of-sight velocity, which we then used to compute σ_{1D} . This measure is shown in the figures as solid black lines, which we compare both to our direct measurement of σ_{LOS} (blue points), as well as σ_{1D} estimated from the best fit from the $nL_{\text{drive}} = 10^{21} \text{ cm}^{-2}$ small-scale simulations ($\sigma_{\text{1D}} \approx \sigma_{\text{LOS}} + 10 \text{ km s}^{-1}$; red triangles). The sightlines used to derive the σ_{LOS} values shown here contained 2 to 5 absorbers on average, with some sightlines having as many as 9 individual absorbers.

A clear radial trend is seen in each panel, with sightlines closer to the simulation centers having larger σ_{LOS} values than those further away, and with the Hydro sightlines tending to have larger velocities overall. This decrease appears to flatten out around 75 kpc, though the spread is still rather large. In both simula-

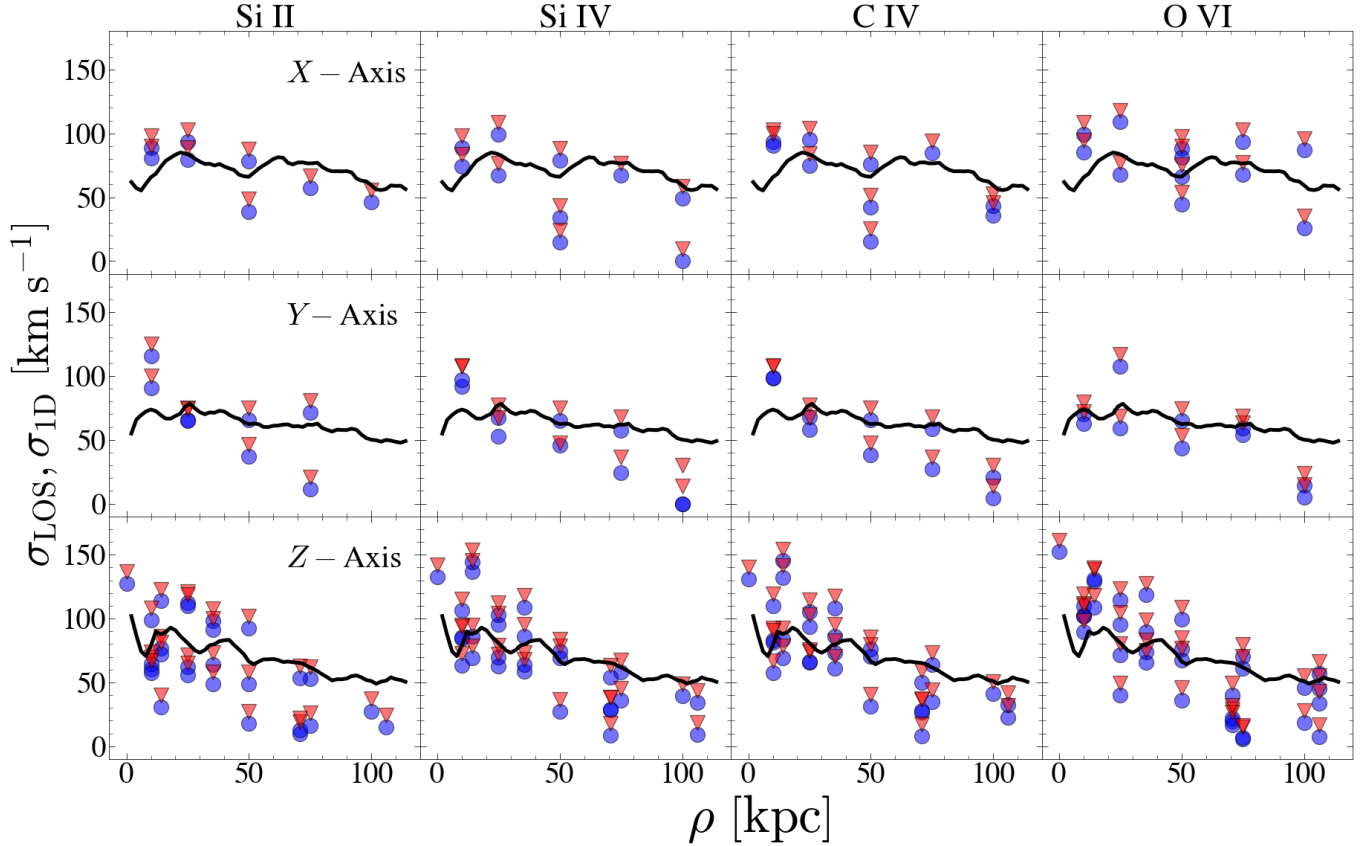


Figure 7. Sightline turbulent measure, σ_{LOS} , in the Hydro simulation as a function of distance from the center of the simulation, ρ . Our measured values are shown in as blue circles while the red triangles shows the measurements after applying the line of best fit from the $nL_{\text{drive}} = 10^{21} \text{ cm}^{-2}$ small-scale simulation. The errors on σ_{LOS} were smaller than the point sizes and so are not shown. Each column corresponds to a different ion, which is labeled at the top while each row corresponds to a different axis being probed by the sightlines. The “true” σ_{LOS} is shown in each panel as a black line as defined in the text.

tions, many of the σ_{LOS} points are found below the true σ_{1D} line, though they do follow the same trend with radius. Applying the line of best fit from the small-scale simulation causes some points in each panel to become roughly consistent with the true σ_{LOS} line in most panels, providing a general estimate of the underlying turbulence, especially in the MHD run. These findings suggest that the actual large-scale turbulent velocities in the CGM are not measured well on a case-by-case basis by σ_{LOS} , but a simple estimate of $\sigma_{\text{1D}} \approx \sigma_{\text{LOS}} + 10 \text{ km s}^{-1}$ provides a reasonable picture of the underlying turbulence on an average basis.

Unlike in the small-scale simulations, we do not see much difference between the gas phases in either the MHD or Hydro simulations. The radial trends are largely the same in each ion, as shown in Figures 7 and 8.

Similar to the small-scale simulations, we generate additional sightlines through the large-scale simulations along their y -axes (i.e., their axes of rotation) and x -axis to determine whether our results are robust to

viewing angle relative to the simulated galaxy. The b_{turb} values from these sightlines are shown in the center and left columns of Figure 6, respectively. These show a slight trend with radius, consistent with what we found along the z -axes. The center and top rows of Figure 7 and 8 show the σ_{LOS} values from these sightlines. These produced a similar radial decline as was seen in our previous results. These indicates that our results are robust to the viewing angle of the sightline.

5.3. Comparison to Observational CGM Surveys

Finally, we compare our large-scale simulations with observational surveys. The b_{turb} measure was employed by Rudie et al. (2019) to constrain the turbulent velocities for 8 galaxies at $z \approx 2$ with stellar masses of $M_{\star} \approx 10^9 - 10^{11} M_{\odot}$ and a median halo mass of $M_{\text{halo}} = 10^{11.9} M_{\odot}$. We find a similar distribution in our MAIHEM simulations, with most components having $b_{\text{turb}} \leq 15 \text{ km s}^{-1}$ and a few being as high as 75 km s^{-1} . While they did not find an anti-correlation with

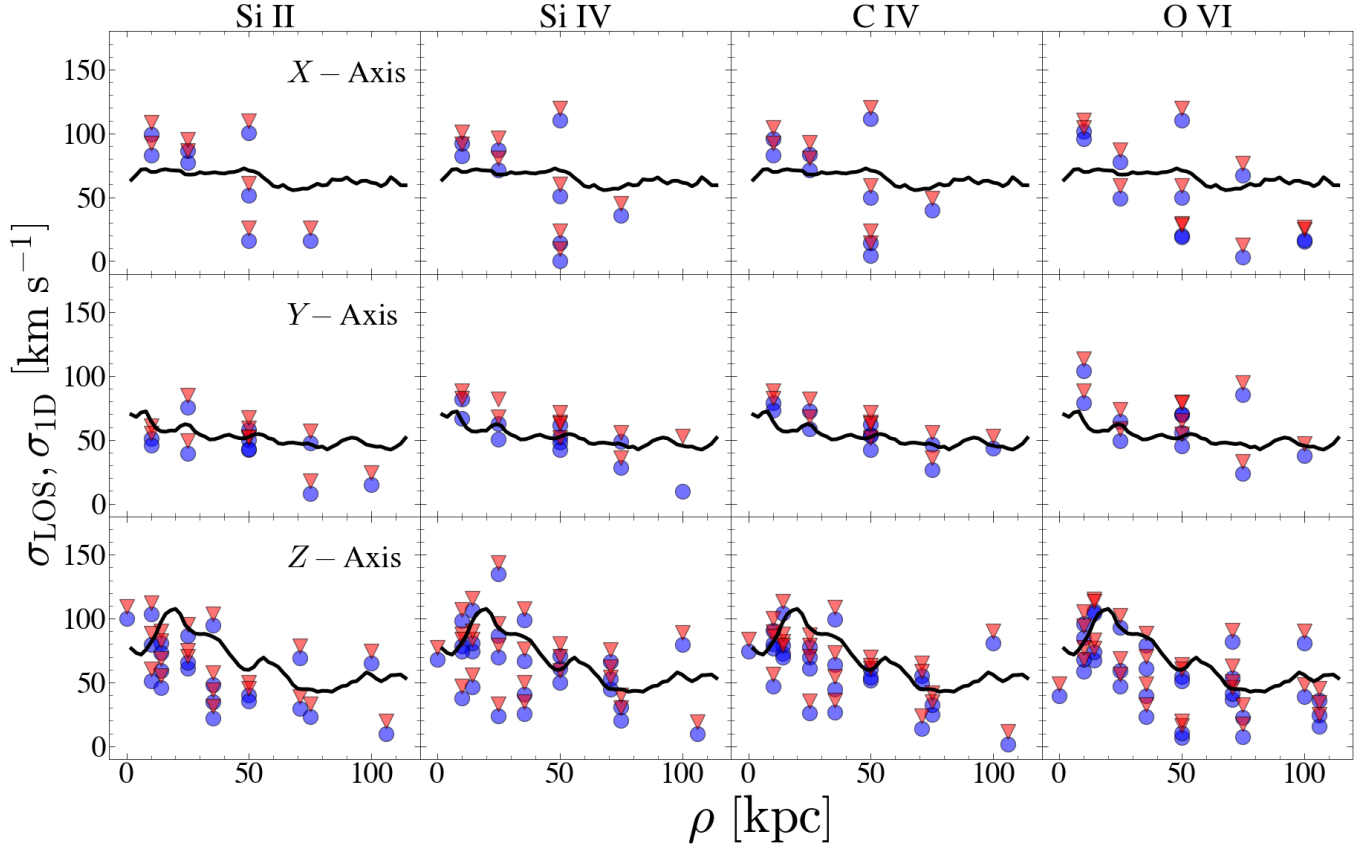


Figure 8. Same as Figure 7 except for the measurements through the MHD simulation.

ρ , they attribute this to the small sample size, stating that the complete sample does show this trend.

Werk et al. (2016) decomposed the Doppler b parameters of their O VI absorbers in the COS-Halos sample into thermal and non-thermal components, as we have done with C IV and Si IV. However, they assume a range of thermal contributions ($6.4 \text{ km s}^{-1} \lesssim b_{\text{therm}}(\text{O VI}) \lesssim 16.2 \text{ km s}^{-1}$) rather than the method we use, described in §4.2. With this, they found an average turbulent velocity range of $\approx 40 - 50 \text{ km s}^{-1}$. While this is higher than the b_{turb} values derived here from the Doppler widths of C IV and Si IV, these are in line with our $\sigma_{\text{LOS}}(\text{O VI})$ velocities in Figures 7 and 8.

Using the velocity centroids of Si II absorbers from the COS-Halos survey (Werk et al. 2013) allows us to compare our σ_{LOS} values to observations, which we show in Figure 9. Both samples show a decrease in $\sigma_{\text{LOS}}(\text{Si II})$ with increasing ρ / R_{vir} , with no absorbers being found beyond $\rho \approx 0.5 R_{\text{vir}}$. Similar velocities were found in each distribution, suggesting the turbulence in our large-scale MAIHEM simulations is comparable to that in the CGM of COS-Halos galaxies.

6. CONCLUSIONS

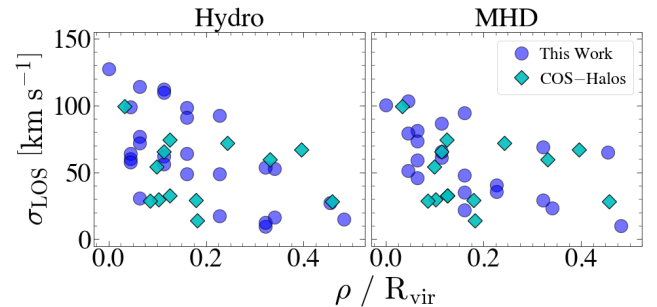


Figure 9. Comparing $\sigma_{\text{LOS}}(\text{Si II})$ measured through the large-scale simulations to the COS-Halos observational survey as a function of impact parameter normalized by the virial radius, ρ / R_{vir} . Blue circles show our measurements through the Hydro and MHD simulations on the left and right panels, respectively while values derived from COS-Halos measurements (Werk et al. 2013) are shown as cyan diamonds.

The properties of the CGM are essential to determining the history of galaxy evolution, but our information about this medium is mostly limited to information inferred from QSO absorption-line measurements. Such measurements uncover a multiphase medium that strongly implies the presence of significant turbulence,

yet the properties of this turbulence remain largely unknown. Here we have analyzed a suite of CGM simulations to determine how well this underlying turbulence relates to two commonly-observed quantities: the non-thermal width of absorption-line components (b_{turb}) and the line-of-sight velocity dispersion between components (σ_{LOS}). Our simulations made use of the MAIHEM code to track non-equilibrium ionization effects, and they consisted both of small-patch and global simulations. This allowed us to probe turbulent motion on both large and small scales, as well as determine how magnetic fields impact σ_{LOS} and b_{turb} .

Our analysis of both types of simulations showed that the turbulence in individual warm absorbers, as measured by b_{turb} , did not trace the turbulent velocities in the media. In our small-scale simulations, the majority of absorbers were narrower than 20 km s^{-1} even in cases in which the overall one-dimensional turbulent velocities were as large as 58 km s^{-1} . Furthermore, the mean b_{turb} did not change with increasing σ_{1D} , though the spread tended to get larger. Kendall τ tests show that b_{turb} and σ_{1D} are not well correlated, likely because b_{turb} measures random motions within individual warm clouds, which do not sample the overall CGM motions. The measure also did a poor job at tracing the turbulent field in the large-scale Hydro simulations, although it was able to show an anti-correlation with radius in the large-scale MHD case, indicative of the declining importance of magnetic pressure at large radii in this simulation.

On the other hand, the line-of-sight velocity dispersion between components, σ_{LOS} , was able to trace the injected turbulence at all scales. In the small-scale simulation with $nL_{\text{drive}} = 10^{21} \text{ cm}^{-2}$, we found that $\sigma_{\text{1D}} \approx \sigma_{\text{LOS}} + 10 \text{ km s}^{-1}$ provided a good description of our results. This trend was shown to be the strongest observed in our study, with a Kendall coefficient of 1. Correlations were also seen in the lower density boxes; however, the trends were somewhat less strong, with σ_{1D} depending more steeply on σ_{LOS} , such that true turbulent velocity dispersion was often underestimated in the less turbulent boxes. On these scales, we find evidence for the trends depending weakly on the gas phase probing σ_{1D} and are robust to viewing angle.

The large-scale simulations, both with and without MHD physics, produced an anti-correlation between ρ and σ_{LOS} that flattened out at $\rho \approx 75 \text{ kpc}$. In these boxes, the measured σ_{LOS} was consistently below the injected turbulence at all ρ , with few exceptions, though

σ_{LOS} and σ_{1D} followed the same radial trend. Unlike in the small-scale simulations, this did not depend on the gas phase being considered. Applying the line of best fit from the small-scale simulation causes some points in each panel to become roughly consistent with the true σ_{1D} line, providing a general estimate of the underlying turbulence, especially in the case of the MHD run. These findings suggest that the actual large-scale turbulent velocities in the CGM are not well measured on a case-by-case basis by σ_{LOS} , but a simple estimate of $\sigma_{\text{1D}} \approx \sigma_{\text{LOS}} + 10 \text{ km s}^{-1}$ provides a reasonable picture of the underlying turbulence on an average basis regardless of viewing angle.

The results from our global simulations are also consistent with those found in recent observations, which indicate that most individual absorbers have $b_{\text{turb}} \leq 15 \text{ km s}^{-1}$, and that the line-of-sight velocity dispersion between absorbers have $10 \text{ km s}^{-1} \lesssim \sigma_{\text{LOS}} \lesssim 150 \text{ km s}^{-1}$, with σ_{LOS} declining strongly with impact parameter. This agreement suggests that the turbulence in our large-scale MAIHEM simulations is comparable to that in the CGM probed by these samples, and that strong correlation between σ_{1D} and σ_{LOS} observed in our study may provide to be useful in analyzing observed systems. Future observational and theoretical studies are needed to help refine our understanding of this connection and its applicability to constraining circumgalactic turbulence with QSO absorption-line measurements.

We would like to acknowledge Sanchayeeta Borthakur and Tyler McCabe for their helpful discussions that greatly improved this manuscript. The simulations used in this work were run on the NASA Pleiades supercomputer maintained by the Science Mission Directorate HighEnd Computing program and the Stampede2 supercomputer at the Texas Advanced Computing Center (TACC) through Extreme Science and Engineering Discovery Environment (XSEDE) resources under grants TGAST130021 and TGPHY200071. E.S. acknowledges support from NASA grant 80NSSC22K1265. The authors acknowledge the native people and the land that Arizona State University's campuses are located in the Salt River Valley. The ancestral territories of Indigenous peoples, including the Akimel O'odham (Pima) and Pee Posh (Maricopa) Indian Communities, whose care and keeping of these lands allows us to be here today.

Software: FLASH (Fryxell et al. 2000; v4.5), matplotlib (Hunter 2007; 3.2.2), yt (Turk et al. 2011), numpy (Harris et al. 2020; v1.22.0), pandas (Reback et al. 2021; 1.3.5)

REFERENCES

- Arav, N., Borguet, B., Chamberlain, C., Edmonds, D., & Danforth, C. 2013, MNRAS, 436, 3286, doi: [10.1093/mnras/stt1812](https://doi.org/10.1093/mnras/stt1812)
- Bordoloi, R., Tumlinson, J., Werk, J. K., et al. 2014, ApJ, 796, 136, doi: [10.1088/0004-637X/796/2/136](https://doi.org/10.1088/0004-637X/796/2/136)

- Borthakur, S., Heckman, T., Tumlinson, J., et al. 2015, *ApJ*, 813, 46, doi: [10.1088/0004-637X/813/1/46](https://doi.org/10.1088/0004-637X/813/1/46)
- . 2016, *ApJ*, 833, 259, doi: [10.3847/1538-4357/833/2/259](https://doi.org/10.3847/1538-4357/833/2/259)
- Buie, Edward, I., Fumagalli, M., & Scannapieco, E. 2020a, *ApJ*, 890, 33, doi: [10.3847/1538-4357/ab65bc](https://doi.org/10.3847/1538-4357/ab65bc)
- Buie, Edward, I., Gray, W. J., & Scannapieco, E. 2018, *ApJ*, 864, 114, doi: [10.3847/1538-4357/aad8bd](https://doi.org/10.3847/1538-4357/aad8bd)
- Buie, Edward, I., Gray, W. J., Scannapieco, E., & Safarzadeh, M. 2020b, *ApJ*, 896, 136, doi: [10.3847/1538-4357/ab9535](https://doi.org/10.3847/1538-4357/ab9535)
- Buie, Edward, I., Scannapieco, E., & Mark Voit, G. 2022, *ApJ*, 927, 30, doi: [10.3847/1538-4357/ac4bc2](https://doi.org/10.3847/1538-4357/ac4bc2)
- Burchett, J. N., Tripp, T. M., Prochaska, J. X., et al. 2015, *ApJ*, 815, 91, doi: [10.1088/0004-637X/815/2/91](https://doi.org/10.1088/0004-637X/815/2/91)
- Burchett, J. N., Tripp, T. M., Prochaska, J. X., et al. 2019, *ApJL*, 877, L20, doi: [10.3847/2041-8213/ab1f7f](https://doi.org/10.3847/2041-8213/ab1f7f)
- Chen, H.-W., Zahedy, F. S., Boettcher, E., et al. 2020, *MNRAS*, 497, 498, doi: [10.1093/mnras/staa1773](https://doi.org/10.1093/mnras/staa1773)
- Chisholm, J., Tremonti, C. A., Leitherer, C., & Chen, Y. 2017, *MNRAS*, 469, 4831, doi: [10.1093/mnras/stx1164](https://doi.org/10.1093/mnras/stx1164)
- Comparat, J., Truong, N., Merloni, A., et al. 2022, *A&A*, 666, A156, doi: [10.1051/0004-6361/202243101](https://doi.org/10.1051/0004-6361/202243101)
- Croton, D. J., Springel, V., White, S. D. M., et al. 2006, *MNRAS*, 365, 11, doi: [10.1111/j.1365-2966.2005.09675.x](https://doi.org/10.1111/j.1365-2966.2005.09675.x)
[x10.48550/arXiv.astro-ph/0508046](https://arxiv.org/abs/10.48550/arXiv.astro-ph/0508046)
- Dekel, A., & Birnboim, Y. 2006, *MNRAS*, 368, 2
- Di Matteo, T., Springel, V., & Hernquist, L. 2005, *Nature*, 433, 604, doi: [10.1038/nature03335](https://doi.org/10.1038/nature03335)
[10.48550/arXiv.astro-ph/0502199](https://arxiv.org/abs/10.48550/arXiv.astro-ph/0502199)
- Eckert, D., Ghirardini, V., Ettori, S., et al. 2019, *A&A*, 621, A40, doi: [10.1051/0004-6361/201833324](https://doi.org/10.1051/0004-6361/201833324)
- Erb, D. K., Li, Z., Steidel, C. C., et al. 2022, *arXiv e-prints*, [arXiv:2210.02465](https://arxiv.org/abs/2210.02465), doi: [10.48550/arXiv.2210.02465](https://doi.org/10.48550/arXiv.2210.02465)
- Fabian, A. C. 2012, *ARA&A*, 50, 455, doi: [10.1146/annurev-astro-081811-125521](https://doi.org/10.1146/annurev-astro-081811-125521)
- Federrath, C., Roman-Duval, J., Klessen, R. S., Schmidt, W., & Mac Low, M. M. 2010, *A&A*, 512, A81, doi: [10.1051/0004-6361/200912437](https://doi.org/10.1051/0004-6361/200912437)
- Fielding, D., Quataert, E., McCourt, M., & Thompson, T. A. 2017, *MNRAS*, 466, 3810, doi: [10.1093/mnras/stw3326](https://doi.org/10.1093/mnras/stw3326)
- Fryxell, B., Olson, K., Ricker, P., et al. 2000, *ApJS*, 131, 273, doi: [10.1086/317361](https://doi.org/10.1086/317361)
- Gray, W. J., & Scannapieco, E. 2016, *ApJ*, 818, 198, doi: [10.3847/0004-637X/818/2/198](https://doi.org/10.3847/0004-637X/818/2/198)
- . 2017, *ApJ*, 849, 132, doi: [10.3847/1538-4357/aa9121](https://doi.org/10.3847/1538-4357/aa9121)
- Gray, W. J., Scannapieco, E., & Kasen, D. 2015, *ApJ*, 801, 107, doi: [10.1088/0004-637X/801/2/107](https://doi.org/10.1088/0004-637X/801/2/107)
- Haardt, F., & Madau, P. 2012, *ApJ*, 746, 125, doi: [10.1088/0004-637X/746/2/125](https://doi.org/10.1088/0004-637X/746/2/125)
- Hamann, F., Kanekar, N., Prochaska, J. X., et al. 2011, *MNRAS*, 410, 1957, doi: [10.1111/j.1365-2966.2010.17575.x](https://doi.org/10.1111/j.1365-2966.2010.17575.x)
- Harris, C. R., Millman, K. J., van der Walt, S. J., et al. 2020, *Nature*, 585, 357, doi: [10.1038/s41586-020-2649-2](https://doi.org/10.1038/s41586-020-2649-2)
- Heckman, T. M., Armus, L., & Miley, G. K. 1990, *ApJS*, 74, 833, doi: [10.1086/191522](https://doi.org/10.1086/191522)
- Hitomi Collaboration, Aharonian, F., Akamatsu, H., et al. 2016, *Nature*, 535, 117, doi: [10.1038/nature18627](https://doi.org/10.1038/nature18627)
- Ho, S. H., Martin, C. L., Kacprzak, G. G., & Churchill, C. W. 2017, *ApJ*, 835, 267, doi: [10.3847/1538-4357/835/2/267](https://doi.org/10.3847/1538-4357/835/2/267)
- Huang, Y.-H., Chen, H.-W., Johnson, S. D., & Weiner, B. J. 2016, *MNRAS*, 455, 1713, doi: [10.1093/mnras/stv2327](https://doi.org/10.1093/mnras/stv2327)
- Hummels, C. B., Smith, B. D., Hopkins, P. F., et al. 2019, *ApJ*, 882, 156, doi: [10.3847/1538-4357/ab378f](https://doi.org/10.3847/1538-4357/ab378f)
- Hunter, J. D. 2007, *Computing in Science and Engineering*, 9, 90, doi: [10.1109/MCSE.2007.55](https://doi.org/10.1109/MCSE.2007.55)
- Kereš, D., & Hernquist, L. 2009, *ApJL*, 700, L1, <https://arxiv.org/abs/0905.2186>
- Kereš, D., Katz, N., Weinberg, D. H., & Davé, R. 2005, *MNRAS*, 363, 2
- Kritsuk, A. G., Norman, M. L., Padoan, P., & Wagner, R. 2007, *ApJ*, 665, 416, doi: [10.1086/519443](https://doi.org/10.1086/519443)
- Lochhaas, C., Bryan, G. L., Li, Y., Li, M., & Fielding, D. 2020, *MNRAS*, 493, 1461, doi: [10.1093/mnras/staa358](https://doi.org/10.1093/mnras/staa358)
- Lochhaas, C., Tumlinson, J., Peeples, M. S., et al. 2022, *arXiv e-prints*, [arXiv:2206.09925](https://arxiv.org/abs/2206.09925), doi: [10.48550/arXiv.2206.09925](https://doi.org/10.48550/arXiv.2206.09925)
- Martin, C. L. 2005, *ApJ*, 621, 227, doi: [10.1086/427277](https://doi.org/10.1086/427277)
- Martin, C. L., Shapley, A. E., Coil, A. L., et al. 2012, *ApJ*, 760, 127
- McNamara, B. R., & Nulsen, P. E. J. 2007, *ARA&A*, 45, 117, doi: [10.1146/annurev.astro.45.051806.110625](https://doi.org/10.1146/annurev.astro.45.051806.110625)
- Meiring, J. D., Tripp, T. M., Werk, J. K., et al. 2013, *ApJ*, 767, 49, doi: [10.1088/0004-637X/767/1/49](https://doi.org/10.1088/0004-637X/767/1/49)
- Moe, M., Arav, N., Bautista, M. A., & Korista, K. T. 2009, *ApJ*, 706, 525, doi: [10.1088/0004-637X/706/1/525](https://doi.org/10.1088/0004-637X/706/1/525)
- Morton, D. C. 2003, *ApJS*, 149, 205, doi: [10.1086/377639](https://doi.org/10.1086/377639)
- Navarro, J. F., Frenk, C. S., & White, S. D. M. 1996, *ApJ*, 462, 563, doi: [10.1086/177173](https://doi.org/10.1086/177173)
- Nicastro, F., Krongold, Y., Fang, T., et al. 2023, *arXiv e-prints*, [arXiv:2302.04247](https://arxiv.org/abs/2302.04247), doi: [10.48550/arXiv.2302.04247](https://doi.org/10.48550/arXiv.2302.04247)
- Ogorzalek, A., Zhuravleva, I., Allen, S. W., et al. 2017, *MNRAS*, 472, 1659, doi: [10.1093/mnras/stx2030](https://doi.org/10.1093/mnras/stx2030)
- Osterman, S., Green, J., Froning, C., et al. 2011, *Ap&SS*, 335, 257, doi: [10.1007/s10509-011-0699-5](https://doi.org/10.1007/s10509-011-0699-5)
- Pan, L., & Scannapieco, E. 2010, *ApJ*, 721, 1765, doi: [10.1088/0004-637X/721/2/1765](https://doi.org/10.1088/0004-637X/721/2/1765)

- . 2011, *PhRvE*, 83, 045302, doi: [10.1103/PhysRevE.83.045302](https://doi.org/10.1103/PhysRevE.83.045302)
- Peeples, M. S., Corlies, L., Tumlinson, J., et al. 2019, *ApJ*, 873, 129, doi: [10.3847/1538-4357/ab0654](https://doi.org/10.3847/1538-4357/ab0654)
- Qu, Z., Chen, H.-W., Rudie, G. C., et al. 2022, *MNRAS*, 516, 4882, doi: [10.1093/mnras/stac2528](https://doi.org/10.1093/mnras/stac2528)
- Rauch, M., Sargent, W. L. W., Womble, D. S., & Barlow, T. A. 1996, *ApJL*, 467, L5, doi: [10.1086/310187](https://doi.org/10.1086/310187)
- Reback, J., Jbrockmendel, McKinney, W., et al. 2021, *pandas-dev/pandas: Pandas 1.3.5, v1.3.5*, Zenodo, Zenodo, doi: [10.5281/zenodo.5774815](https://doi.org/10.5281/zenodo.5774815)
- Rubin, K. H. R., Prochaska, J. X., Koo, D. C., & Phillips, A. C. 2012, *ApJL*, 747, L26, <https://arxiv.org/abs/1110.0837>
- Rudie, G. C., Steidel, C. C., Pettini, M., et al. 2019, *ApJ*, 885, 61, doi: [10.3847/1538-4357/ab4255](https://doi.org/10.3847/1538-4357/ab4255)
- Rudie, G. C., Steidel, C. C., Trainor, R. F., et al. 2012, *ApJ*, 750, 67, doi: [10.1088/0004-637X/750/1/67](https://doi.org/10.1088/0004-637X/750/1/67)
- Scannapieco, E. 2017, *ApJ*, 837, 28, doi: [10.3847/1538-4357/aa5d0d](https://doi.org/10.3847/1538-4357/aa5d0d)
- Scannapieco, E., & Brügggen, M. 2015, *ApJ*, 805, 158, doi: [10.1088/0004-637X/805/2/158](https://doi.org/10.1088/0004-637X/805/2/158)
- Scannapieco, E., & Oh, S. P. 2004, *The Astrophysical Journal*, 608, 62–79, doi: [10.1086/386542](https://doi.org/10.1086/386542)
- Schmidt, W., Federrath, C., Hupp, M., Kern, S., & Niemeyer, J. C. 2009, *A&A*, 494, 127, doi: [10.1051/0004-6361:200809967](https://doi.org/10.1051/0004-6361:200809967)
- Steidel, C. C., Erb, D. K., Shapley, A. E., et al. 2010, *ApJ*, 717, 289, doi: [10.1088/0004-637X/717/1/289](https://doi.org/10.1088/0004-637X/717/1/289)
- Stewart, K. R., Kaufmann, T., Bullock, J. S., et al. 2011, *ApJ*, 738, 39, <https://arxiv.org/abs/1103.4388>
- Thacker, R. J., Scannapieco, E., & Couchman, H. M. P. 2006, *ApJ*, 653, 86, doi: [10.1086/50865010.48550/arXiv.astro-ph/0606214](https://doi.org/10.1086/50865010.48550/arXiv.astro-ph/0606214)
- Thompson, T. A., Quataert, E., Zhang, D., & Weinberg, D. H. 2016, *MNRAS*, 455, 1830, doi: [10.1093/mnras/stv2428](https://doi.org/10.1093/mnras/stv2428)
- Tripp, T. M., Meiring, J. D., Prochaska, J. X., et al. 2011, *Science*, 334, 952, doi: [10.1126/science.1209850](https://doi.org/10.1126/science.1209850)
- Tumlinson, J., Peeples, M. S., & Werk, J. K. 2017, *ARA&A*, 55, 389, doi: [10.1146/annurev-astro-091916-055240](https://doi.org/10.1146/annurev-astro-091916-055240)
- Tumlinson, J., Thom, C., Werk, J. K., et al. 2013, *ApJ*, 777, 59, doi: [10.1088/0004-637X/777/1/59](https://doi.org/10.1088/0004-637X/777/1/59)
- Turk, M. J., Smith, B. D., Oishi, J. S., et al. 2011, *ApJS*, 192, 9, doi: [10.1088/0067-0049/192/1/9](https://doi.org/10.1088/0067-0049/192/1/9)
- Uhlenbeck, G. E., & Ornstein, L. S. 1930, *Physical Review*, 36, 823, doi: [10.1103/PhysRev.36.823](https://doi.org/10.1103/PhysRev.36.823)
- van de Voort, F., Springel, V., Mandelker, N., van den Bosch, F. C., & Pakmor, R. 2019, *MNRAS*, 482, L85, doi: [10.1093/mnrasl/sly190](https://doi.org/10.1093/mnrasl/sly190)
- Veilleux, S., Cecil, G., & Bland-Hawthorn, J. 2005, *ARA&A*, 43, 769, doi: [10.1146/annurev.astro.43.072103.150610](https://doi.org/10.1146/annurev.astro.43.072103.150610)
- Voit, G. M., Bryan, G. L., O’Shea, B. W., & Donahue, M. 2015, *ApJL*, 808, L30, doi: [10.1088/2041-8205/808/1/L30](https://doi.org/10.1088/2041-8205/808/1/L30)
- Werk, J. K., Prochaska, J. X., Thom, C., et al. 2013, *ApJS*, 204, 17, doi: [10.1088/0067-0049/204/2/17](https://doi.org/10.1088/0067-0049/204/2/17)
- Werk, J. K., Prochaska, J. X., Tumlinson, J., et al. 2014, *ApJ*, 792, 8, doi: [10.1088/0004-637X/792/1/8](https://doi.org/10.1088/0004-637X/792/1/8)
- Werk, J. K., Prochaska, J. X., Cantalupo, S., et al. 2016, *ApJ*, 833, 54, doi: [10.3847/1538-4357/833/1/54](https://doi.org/10.3847/1538-4357/833/1/54)
- Werner, N., Zhuravleva, I., Churazov, E., et al. 2009, *MNRAS*, 398, 23, doi: [10.1111/j.1365-2966.2009.14860.x](https://doi.org/10.1111/j.1365-2966.2009.14860.x)
- Zahedy, F. S., Chen, H.-W., Cooper, T. M., et al. 2021, *MNRAS*, 506, 877, doi: [10.1093/mnras/stab1661](https://doi.org/10.1093/mnras/stab1661)
- Zhu, G., Ménard, B., Bizyaev, D., et al. 2014, *MNRAS*, 439, 3139, doi: [10.1093/mnras/stu186](https://doi.org/10.1093/mnras/stu186)
- Zhuravleva, I., Allen, S. W., Mantz, A., & Werner, N. 2018, *ApJ*, 865, 53, doi: [10.3847/1538-4357/aadae3](https://doi.org/10.3847/1538-4357/aadae3)